Appl Phys B (2011) 103: 195–205
DOI 10.1007/s00340-010-4197-1

Applied Physics B
Lasers and Optics

Modeling of ultrashort pulsed laser ablation in water and biological tissues in cylindrical coordinates

J. Jiao · Z. Guo

Received: 17 May 2010 / Revised version: 29 July 2010 / Published online: 16 September 2010

Abstract A numerical model combining the ultrafast radiative transfer and the ablation rate equation is proposed to investigate the transient process of plasma formation during laser plasma-mediated ablation of absorbing-scattering media. The focus beam propagation governed by the transient equation of radiative transfer is solved by the transient discrete ordinates method to account for scattering effect. The temporal evolution of the free-electron density governed by the ablation rate equation is calculated using a fourth-order Runge–Kutta method to examine various effects such as the multiphoton, chromophore, and cascade ionizations. The threshold of optical breakdown, the shape and maximum length of plasma growth for ablation in water are predicted by the present model and compared with the existing experimental and numerical data. Good agreements have been found. The dynamic process of plasma formation for ablation in the model skin tissue is simulated. A parametric study with regard to the influences of the ionization energy and the critical free-electron density on the ablation threshold of the tissue is conducted.

1 Introduction

There has been an increasing demand of lasers in surgical and medical procedures in recent years. The use of highly focused pulsed laser beam to modify and manipulate biological media for applications in molecular and cellular biophysics and biotechnology becomes more pervasive [1, 2]. Applications include dissection or inactivation of cellular organelles, cytoskeletal filaments, and chromosomes with submicron spatial precision [3], sampling of heterogeneous systems via laser pressure catapulting [4], and gene delivery through transient membrane disruption (optoporation) [5], to name a few. As the pulsed laser microbeam technologies continue to advance, the fundamental knowledge of laser-tissue interaction mechanisms is of vital importance and could provide a framework wherein systematic investigation of novel pulsed microbeam techniques can be explored and developed.

Three major models including the selective photothermolysis model, the photochemical model, and the plasma-mediated ablation model, have emerged to elucidate various laser ablation mechanisms. The selective photothermolysis model [6] has been proposed and used as a guide to estimate the relation between the collateral tissue damage and laser parameter for both short and long laser pulses [7]. In this model, ablation is attributed to a result of rapid vaporization due to the absorption of laser power in tissue. The photochemical model conjectures the pressure increase as a result of photochemical dissociation of the macromolecular bonds due to the large photon energy of the deep ultraviolet (UV) light [8]. These two models assume strong light absorption by the chromorphores in selected spectral bands as the cause of tissue ablation without considering the possibility of laser-induced ionization or plasma generation. In contrast, the latest plasma-mediated ablation model has been employed to explain the optical breakdown phenomenon in the visible and near-infrared wavelength region, in which plasma induced by the strong electromagnetic field of a short laser pulse without significant light absorption, is considered as the cause of breakdown [1, 9–12].

Laser plasma-mediated ablation, also known as laser induced optical breakdown, occurs when a specific irradiance

J. Jiao · Z. Guo (✉)
Department of Mechanical and Aerospace Engineering, Rutgers, The State University of New Jersey, Piscataway, NJ 08854, USA
e-mail: guo@jove.rutgers.edu
Fax: +1-732-4453124

threshold is exceeded. In this model, the temporal evolution of free electrons (i.e. plasmas) is predicted by a rate equation and the threshold is determined as the calculated free-electron density is equal to a critical value. Initial work to illustrate the underlying mechanisms of the plasma-induced ablation was conducted in distilled water since water is the dominant component by weight for most human tissues. Multiphoton ionization is most likely the pathway for generating seed electrons for cascade ionization, which is dominant in the optical breakdown process in water [9].

Plasma formation is characterized by the growth of plasmas. Docchio et al. [13, 14] proposed the "moving breakdown" model to analyze plasma starting times and the temporal and spatial dynamics of plasma expansion in liquids subject to nanosecond laser pulse irradiation. Fan et al. [15] modified the model by taking into account the pulse propagation to characterize the time and space dependent breakdown region induced by femtosecond laser pulses. Recently, Zhou et al. [16] used the rate equation to investigate the transient progression of plasma in pure water generated by focused short laser pulses. However, all the works mentioned above simplified the distilled water as a one-dimensional (1-D) computational domain.

Nevertheless, real tissues differ from distilled water in both mechanical and electronic properties due to the complex nature of tissue. Although the pure water can be well-approximated as an amorphous semiconductor with an energy band gap 6.5 eV [17], tissues contain many molecules with energy level inside the water band gap. These defects may play an important role in plasma formation [18]. It is also noticed that chromophore ionization pathway is incorporated in a recent model [19] to explain the skin tissue ablation by nanosecond laser pulses to resolve significant light absorption.

To induce plasma ablation, use of ultrashort pulsed (USP) lasers with pulse duration down to picoseconds or femtoseconds is required. Due to the extreme short pulse duration, USP laser beam interaction with tissue occurs before thermal diffusion ever takes place, leading to precise ablation with minimized thermal and collateral damage [20–23]. Yamada [24, 25] and Mitra and Kumar [26] are pioneers in the modeling of photon transport and migration in turbid media like tissues, whose work employed either diffusion approximation [24, 25] or 1-D radiative transfer model [26]. Biological tissues are generally highly scattering against laser irradiation. A two-dimensional (2-D) axisymmetric modeling of the laser pulse transient radiation propagation and transport [27] is thus required to accurately predict the temporal and spatial laser intensity distribution in turbid tissues. Guo's group is well known in developing multi-dimensional ultrafast radiative transfer methods including the transient discrete ordinates method [28, 29], the transient Monte Carlo method [30], and the transient radiation element method [31]. Guo et al. [32] also conducted experimental measurements to validate the modeling. Recently, Guo's group investigated plasma-induced ablation [22, 23] as well as thermal interaction [33] of focused short laser pulses with skin tissues.

In this treatise, a theoretical model which combines the transient radiative transfer and the rate equation is developed to simulate the dynamic process of plasma formation in the ablation of participating media. To validate the proposed model, the plasma-induced optical breakdown in distilled water is first studied; in which the ablation threshold, the shape and length of the plasma formation calculated by the present model are compared with the experimental data and other numerical models available in the literature. Then the ablation of biological tissues with pico- and femtosecond laser pulses is investigated. The model tissue is an axisymmetric cylinder and is stratified as three layers with different optical properties similar to human skin tissues—epidermis, dermis, and subcutaneous fat, respectively. The ultrashort laser pulse is converged inside the skin tissue to induce plasma breakdown for ablating cancerous tissue. The intensity of the focused beam is calculated by solving the transient equation of radiative transfer, and the space and time-dependent free-electron density is obtained according to the laser irradiance profile. Various ionization mechanisms such as multiphoton, chromophore and cascade ionization are examined to show their effects on tissue ablation. The temporal evolution of the free-electron density is also illustrated at different locations inside the skin tissue. Finally, we conclude with a discussion of the influences of the ionization energies and the critical free-electron densities on the ablation threshold in human skin tissues.

2 Numerical models

2.1 Focused laser beam

A converging laser beam is sketched in Fig. 1, in which the beam radius $(1/e^2)$ at distance z from the beam focus can be expressed as

$$w(z) = w_{0\mathrm{R}}\left[1 + \left(\frac{z}{z_{\mathrm{R}}}\right)^2\right]^{1/2}, \tag{1}$$

where $w_{0\mathrm{R}}$ is the beam waist at the focus; and z_{R} is Rayleigh length calculated by

$$z_{\mathrm{R}} = \frac{n\pi w_{0\mathrm{R}}^2}{M^2\lambda}. \tag{2}$$

Here, n is the refractive index of the medium; λ the laser wavelength in free space; M^2 the beam quality factor defined as

$$M^2 = \frac{w_{0\mathrm{R}}\theta_{\mathrm{R}}}{w_0\theta}. \tag{3}$$

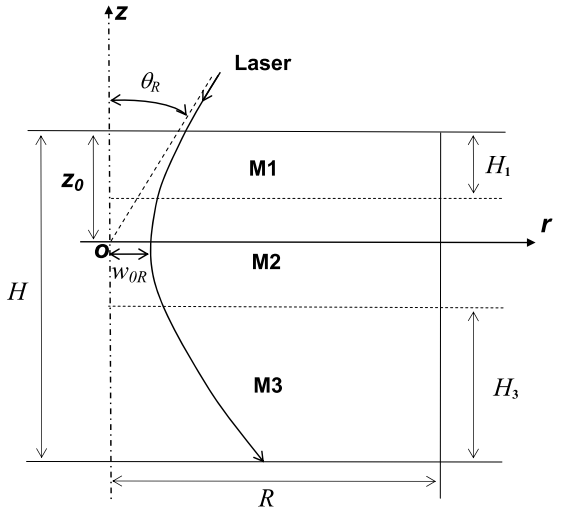

Fig. 1 Sketch of the geometric coordinates and dimensions

Here, θ_{R} is the far-field divergence of a real beam; w_0 and θ the beam waist and far-field divergence of a true Gaussian beam, respectively. For a truly Gaussian beam, $M^2 = 1$.

The radiation intensity has two components: the ballistic component I^{b} accounting for the incident laser beam and the diffuse component I^{d} standing for the scattering component of the laser beam in a scattering medium like a biological tissue. The distribution of I^{b} for a laser beam having a Gaussian profile both temporally and spatially is described by the Beer–Lambert law as [27, 33]

$$I^{\mathrm{b}}(r,z,t) = I_0(z)\exp\left\{-4\ln 2\left[\left(t-\frac{|z-z_0|}{c\cos\theta}\right)\Big/ t_{\mathrm{p}}-2\right]^2\right\} \times \exp\left[-\frac{2r^2}{w(z)^2}\right]\exp\left(-\frac{\sigma_{\mathrm{e}}|z-z_0|}{\cos\theta}\right), \tag{4}$$

where c is the speed of light in the medium; θ is the angle between the incident laser and the optical axis; t_{p} is the pulse width at half maximum; σ_{e} is the extinction coefficient, which is the summation of the absorption coefficient σ_{a} and the scattering coefficient σ_{s}; The total time duration of a whole pulse is set as $4t_{\mathrm{p}}$ in this study, so that the peak of the pulse arrives at time $2t_{\mathrm{p}}$.

Since the laser power, P, incident in a medium without attenuation is a constant, it follows that

$$P = \int_0^{\infty} I_0(z)\exp\left[-\frac{2r^2}{w(z)^2}\right]2\pi r\,dr. \tag{5}$$

Therefore, the amplitude of the beam radiation strength $I_0(z)$ can be specified using

$$I_0(z) = \frac{2P}{\pi w(z)^2}. \tag{6}$$

The diffuse intensity I_l^{d} in a discrete ordinate $\vec{s}_l$ is governed by the transient equation of radiative transfer in the cylindrical coordinates [27]:

$$\frac{1}{c}\frac{\partial I_l^{\mathrm{d}}}{\partial t} + \frac{\mu_l}{r}\frac{\partial}{\partial r}\left(rI_l^{\mathrm{d}}\right) - \frac{1}{r}\frac{\partial}{\partial\phi}\left(\eta_l I_l^{\mathrm{d}}\right) + \xi_l\frac{\partial I_l^{\mathrm{d}}}{\partial z} + \sigma_{\mathrm{e}}I_l^{\mathrm{d}} = \sigma_{\mathrm{e}}S_l, \quad l = 1,2,\ldots,N, \tag{7}$$

where μ_l, η_l, ξ_l are the three directional cosines; N is the total number of discrete directions; and S_l is the radiative source term expressed as

$$S_l = (1-\omega)I_{\mathrm{b}} + \frac{\omega}{4\pi}\sum_{j=1}^{N} w_j\Phi_{jl}I_j^{\mathrm{d}} + S^{\mathrm{b}}, \tag{8}$$

where I_{b} is the blackbody emitting intensity of the medium; $\omega = \sigma_{\mathrm{s}}/(\sigma_{\mathrm{s}}+\sigma_{\mathrm{a}})$ is the scattering albedo; w_j is the appropriate angular weight in discrete direction $\vec{s}_j$; Φ_{jl} represents the scattering phase function $\Phi(\vec{s}_j \to \vec{s}_l)$; S^{b} is the source contribution of the laser irradiation:

$$S^{\mathrm{b}} = \frac{\omega}{4\pi}I^{\mathrm{b}}\Phi(\vec{s}_{\mathrm{b}} \to \vec{s}_l). \tag{9}$$

The unit vector $\vec{s}_{\mathrm{b}}$ represents the laser incident direction. In the region where no laser irradiation is passing through, $I^{\mathrm{b}} = S^{\mathrm{b}} = 0$.

In the present study, scaling isotropic scattering [34, 35] is considered though the current model is capable of dealing with anisotropic scattering. Thus, we have $\Phi(\vec{s}_j \to \vec{s}_l) = 1$ and σ_{s} is the reduced scattering coefficient. The blackbody emission from the medium is negligible as compared with the powerful laser intensity. Once plasma is generated, the local medium properties ($\sigma_{\mathrm{a}}, \sigma_{\mathrm{s}}, \sigma_{\mathrm{e}}$, and ω) in (4)–(9) should be modified to include the plasma absorption coefficient and the possible change in the scattering coefficient because of the modification to the index of refraction due to free-electron ejection in a neutral medium. In the present studies, we only considered the superposition of plasma absorption and neglected change in scattering coefficient.

Once the intensity field is obtained, the incident radiation is calculated as [28, 29]

$$G = \sum_{l=1}^{N} w_l I_l^{\mathrm{d}} + I^{\mathrm{b}}. \tag{10}$$

The incident radiation is the total intensity impinging on a point from all directions. For an extremely weakly-scattering medium like pure water, the value of the incident radiation equals to the ballistic laser irradiance, I^{b}.

2.2 Temporal evolution of plasmas

The time evolution of the free-electron density in a control volume can, in a simplified way, be described by a modified rate equation in a generic form:

$$\frac{\partial \rho}{\partial t} = \left(\frac{\partial \rho}{\partial t}\right)_{\mathrm{mp}} + \left(\frac{\partial \rho}{\partial t}\right)_{\mathrm{ch}} + \eta_{\mathrm{casc}}\rho - g\rho - \eta_{\mathrm{rec}}\rho^2, \quad (11)$$

where the free-electron density ρ is a function of time. The first three terms on the right hand side represent the production of free electrons through multiphoton, chromophore and cascade ionizations, respectively. The last two terms are the electron losses through diffusion and recombination, respectively. The cascade ionization rate and the diffusion rate are proportional to the number of the existing free electrons. The recombination rate is proportional to ρ^2, as it involves an interaction between two charged particles (an electron-hole pair) [9].

2.2.1 Multiphoton ionization

To ionize an atom or molecule with ionization energy ΔE, the number of photons required is $k = \langle \Delta E/(\hbar\omega) + 1 \rangle$; in which $\hbar$ is the Planck constant and $\omega = 2\pi c/\lambda$ is the laser circular frequency. From the viewpoint of quantum mechanics, the possibility for generating a free electron through multiphoton ionization will decrease as the laser wavelength increases. An approximate expression for the multiphoton ionization rate is derived as [36]

$$\left(\frac{\partial \rho}{\partial t}\right)_{\mathrm{mp}} \approx \frac{2\omega}{9\pi}\left(\frac{m'\omega}{\hbar}\right)^{3/2}\left[\frac{e^2}{16m'\Delta E\omega^2 c\varepsilon_0 n}G\right]^k \times \exp(2k)\varphi\left(\sqrt{2k - \frac{2\Delta E}{\hbar\omega}}\right), \quad (12)$$

where an electron charge is $e = 1.6022 \times 10^{-19}$ C; m is the mass of electron; $m' = \frac{m}{2}$ is the reduced excitation mass; ε_0 is the vacuum permittivity, and $\varphi(x)$ expresses the Dawson function:

$$\varphi(x) = \exp\left(-x^2\right)\int_0^x \exp\left(y^2\right) dy. \quad (13)$$

The ionization energy is $\Delta E = 6.5$ eV for water [17] and $\Delta E = 4.6$ eV for skin tissue [19], respectively.

2.2.2 Chromophore ionization

A necessary condition for the chromophore ionization pathway in generating quasi-free electrons lies in adiabatic heating of the chromophores by the ultrashort laser pulses. The characteristic time of thermal energy transporting out of an illuminated chromophore is estimated to be 20 μs [19]. Hence, the adiabatic heating condition can be assumed for the picosecond or femtosecond laser interaction with the tissue.

The quasi-free-electron density due to chromophore ionization is represented as [19]

$$\rho_{\mathrm{ch}}(t) = \frac{3\sqrt{\pi}n_{\mathrm{ch}}N_{\mathrm{b}}}{4}\left[\frac{2k_{\mathrm{B}}}{\Delta E}\left(T_0 + \frac{F(t)\sigma_{\mathrm{a}}}{c_{\mathrm{ch}}\rho_{\mathrm{ch}}f_{\mathrm{ch}}}\right)\right]^{\frac{3}{2}} \times \exp\left\{-\frac{\Delta E}{2k_{\mathrm{B}}[T_0 + \frac{F(t)\sigma_{\mathrm{a}}}{c_{\mathrm{ch}}\rho_{\mathrm{ch}}f_{\mathrm{ch}}}]}\right\}, \quad (14)$$

where $F(t) = \int_0^t G(t)\,dt$ is the time integral of the incident radiation; $n_{\mathrm{ch}} \approx 1 \times 10^{15}$ m^{-3} is the number density of chromophores in skin tissue; $N_{\mathrm{b}} \approx 1.0 \times 10^{11}$ is the average number of bound electrons per chromophore; k_{B} is the Boltzmann constant; T_0 is the ambient temperature assumed to be 300 K; $c_{\mathrm{ch}} = 2.51 \times 10^3$ J/(kg K) is the specific heat of melanosome organelles; $f_{\mathrm{ch}} \approx 0.5\%$ is the volume ratio of the chromophore to skin [19]. By taking a partial derivative of the free-electron density with respect to time, the chromophore ionization rate is obtained.

2.2.3 Cascade ionization

As soon as a free electron exists in the interaction volume, it gains energy from the electric field through inverse bremsstrahlung absorption (*IBA*) of photons and can generate further free electrons through impact ionization. Conservation of momentum requires that the absorption of photons from the laser pulse takes place during collisions of the free electrons with the surrounding molecules. The cascade ionization rate coefficient η_{casc} is given by [36]

$$\eta_{\mathrm{casc}} = \frac{1}{\omega^2\tau^2 + 1}\left(\frac{e^2\tau}{c\varepsilon_0 nm\Delta E}G - \frac{m\omega^2\tau}{M_{\mathrm{m}}}\right). \quad (15)$$

Here, $\tau \approx 1$ fs is the time of collision between an electron and a heavy particle; M_{m} is the mass of molecule with $M_{\mathrm{m}} \approx 3 \times 10^{-26}$ kg for water and $M_{\mathrm{m}} \approx 2 \times 10^{-16}$ kg for chromophores [19].

The onset of cascade ionization requires the presence of "seed electrons" in the conduction band. In this study, cascade ionization was assumed to occur after one initial free electron is present in the calculation control volume [36].

2.2.4 Diffusion and recombination

The diffusion of electrons from the focal volume was estimated by approximating the focal volume as a cylinder of radius w_0 and length z_{R}. Thus, the diffusion rate per electron is expressed as [36]

$$g = \frac{\tau\Delta E}{3m}\left[\left(\frac{2.4}{w_{0\mathrm{R}}}\right)^2 + \left(\frac{1}{z_{\mathrm{R}}}\right)^2\right]. \quad (16)$$

Table 1 Optical properties of the skin tissues at wavelength 1064/1552 nm [39]

Tissue type	Epidermis	Dermis	Fat
σ_a (mm^{-1})	0.02/1.85	0.05/0.90	0.07/0.52
σ_s (mm^{-1})	3.0/2.2	1.83/1.73	1.69/1.67

The recombination rate η_{rec} is considered as 2×10^{-9} cm^3/s [37].

2.3 Properties of the media

For consistent comparison with other numerical models, the distilled water at the wavelengths considered in this paper such as 532, 580 and 1064 nm is treated as a transparent medium. There are no chromophore ionization, absorption and scattering of light. The normalized laser energy is defined as $\beta = E/E_{th}$, where E_{th} is the energy threshold for a single pulse. A spatially and temporally constant absorption coefficient of the plasmas generated by the pulsed laser is assumed. The plasma absorption coefficient is adopted as $\sigma_{ap} = 180$ cm^{-1} for 300 fs pulses with a normalized energy value $\beta = 10$ [15]; and $\sigma_{ap} = 360$ cm^{-1} for 30 ps pulses with $\beta = 20$ [38].

The model tissue cylinder is shown in Fig. 1, with dimensions $H = 5$ mm and $R = 5$ mm. The origin of the coordinates is always located at the focal spot center of the incident laser beam. The cylindrical coordinate variables are z and r. The model tissue is stratified as three different layers with different physical properties similar to a skin tissue. The first layer is epidermis ($H_1 = 0.5$ mm). The last layer is subcutaneous fat ($H_3 = 3.0$ mm). In between is the dermis ($H_2 = H - H_1 - H_3 = 1.5$ mm). Usually the skin cancerous cells are developed from the basal layer—the interface between the epidermis and dermis layers. A laser beam is then assumed to be converged to a small spot at the basal layer by a single objective lens. The optical properties of the skin tissues at wavelengths 1064/1552 nm [39] are listed in Table 1. The refractive index of the tissues is assumed to be constant at 1.40 [40]. For water, the refractive index used in the calculations is 1.33.

2.4 Numerical scheme

The transient discrete ordinates method (*TDOM*) with the S_{12} scheme was employed for the solution of the present transient equation of radiative transfer. This numerical method has been well discussed in Guo's previous publications [27, 29]; and thus, the details are not repeated here. The evolution of free electron density subject to laser irradiation is obtained by solving the rate equation with a fourth-order Runge–Kutta method.

To improve the numerical calculation efficiency and to capture the rapid change in the focal spot, a non-uniform grid system is employed with refined grids in the focal region. For the considered medium cylinder with $H = 5$ mm and $R = 5$ mm, a staggered grid of 200×100 is adopted in the present calculations. Because the minimum grid size is around 1.0 μm, the time step is restricted to a value less than 5 fs [29] for the ultrafast radiative transfer analysis. The same time step is adopted for solving the rate equation with a fourth-order Runge–Kutta method. For the 30 ps pulses, a time step 4 fs is selected for the calculations; while for the 300 and 900 fs pulses, a time step 0.5 fs is chosen. Several sets of different grid sizes and time steps were considered to give satisfactory convergent results.

In the present computation, a DELL PC (OPTIPLEX 755: 2.40 GHz CPU and 3.25 GB RAM) is used. It takes half-hour to dozens of hours in the calculation depending on the specified gird size and the angular discretization scheme.

3 Results and discussion

The present model is validated in Table 2 via comparing the thresholds of optical breakdown in distilled water calculated by the present code (I_{th4}) with the experimental data (I_{exp}) reported by Vogel et al. [41] and the numerical values in the papers of Noack and Vogel [9] (I_{th1}), Sollier et al. [42] (I_{th2}) and Zhou et al. [16] (I_{th3}). In the numerical models, the optical breakdown in the distilled water is identified when the maximum free-electron density generated at the focal spot center during the period of one laser pulse equals to a critical electron density. Two critical electron densities ($\rho_{cr} = 10^{20}$ cm^{-3} and $\rho_{cr} = 10^{21}$ cm^{-3}) were considered. Equation (11) was iteratively solved for different amplitudes of the radiation strength at the focal plane $I_0(z = 0)$ until the optical breakdown is induced, and this amplitude is defined as the breakdown threshold I_{th}.

A good agreement is found between the present results (I_{th4}) and the numerical results from the other groups (I_{th1}, I_{th2} and I_{th3}) at all the considered wavelengths and pulse durations. The slight differences between the different models can be attributed to the 2-D axisymmetric cylindrical model in the present calculations and the 1-D model by others as well as the possible differences in the Runge–Kutta algorithm as identified in Ref. [16].

For ablation with the 6 ns pulses at both wavelengths 580 and 1064 nm, the predicted thresholds (I_{th1}, I_{th2}, I_{th3} and I_{th4}) under the assumption $\rho_{cr} = 10^{20}$ cm^{-3} give a better agreement with the measured threshold (I_{exp}). For ablation with the picosecond pulses (3 ps and 30 ps) and the femtosecond pulses (100 fs and 300 fs), at all the three wavelengths 532, 580 and 1064 nm, the cases with $\rho_{cr} = 10^{21}$ cm^{-3} yield a better agreement between the numerical and

Table 2 Comparison of the breakdown thresholds predicted by the present model (I_{th4}) with the numerical and experimental results in the literature (I_{exp}—quoted from Vogel et al. [41]; I_{th1}—quoted from Noack and Vogel [9]; I_{th2}—quoted from Sollier et al. [42]; I_{th3}—quoted from Zhou et al. [16]). The unit for irradiance is 10^{10} W/cm^2

λ	t_p	$2w_0$		$\rho_{cr} = 10^{20}$ cm^{-3}				$\rho_{cr} = 10^{21}$ cm^{-3}			
nm	ps	μm	I_{exp}	I_{th4}	I_{th3}	I_{th2}	I_{th1}	I_{th4}	I_{th3}	I_{th2}	I_{th1}
532	6000	5.3	3.0	4.0	4.0	4.1	4.0	35.7	35.9	36.0	36.0
532	30	3.4	38	9.3	9.3	9.5	9.0	35.7	35.9	36.0	36.0
580	3	5.0	85	71.7	71.5	75.1	72.0	91.4	91.6	95.2	92.0
580	0.3	5.0	476	406.3	410.0	439.3	400.0	514.0	513.2	547.3	510.0
580	0.1	4.4	1110	845.1	844.1	931.4	826.0	1114.5	1113.6	1209.2	1090
1064	6000	7.7	5.0	3.2	3.0	3.5	5.0	10.9	10.9	10.9	11.0
1064	30	4.7	45	10.2	10.3	11.7	10.0	12.3	13.1	14.0	13.0

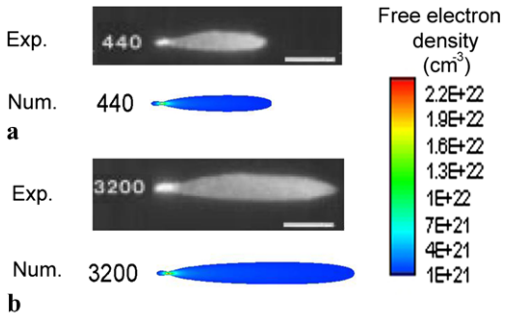

Fig. 2 Comparison of the formed plasma shapes between the present modeling and the experimental photos in Ref. [41] for ablation in water with a 30 ps pulse at wavelength 1064 nm: (**a**) plasma formed at pulse energy 440 μJ; and (**b**) plasma formed at pulse energy 3200 μJ. The laser is incident from the right. The bar represents a length of 100 μm

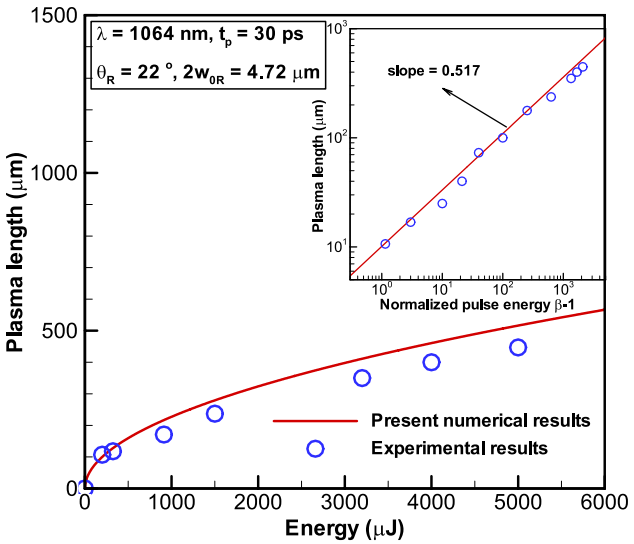

Fig. 3 Plots of the plasma length as a function of the laser pulse energy (the experimental results are from Ref. [41])

the experimental results. Therefore, the critical free-electron density is selected as $\rho_{cr} = 10^{21}$ cm^{-3} in the following calculations concerning the ablation in water induced by the picosecond and femtosecond lasers.

An advantage of the present model over the other numerical models above-mentioned is that it is able to simulate the temporal and spatial plasma formation. Figure 2 compares the simulated plasma formations with the experimental observations for two different pulse energies 440 and 3200 μJ, respectively. The laser pulse is 30 ps at wavelength 1064 nm with a constant focusing angle 22°. The laser beam was converged to a focal spot $2w_{0R} = 4.7$ μm inside the distilled water. The experimental pictures of the luminescent plasmas were taken with an open shutter in a dark room by Vogel et al. [41]. The numerical pictures are obtained by calculating the time average of the accumulated free electrons during the breakdown period. As shown in Fig. 2, the formed plasma clouds predicted by the present numerical model match very well with the experimental pictures. It should be pointed out that the plasma luminescence pictures taken in the experiment may not reflect the exact boundary of plasmas; while the critical plasma density value set in the simulation is also an assumption.

Figure 3 compares the plasma lengths in water between the present simulation and the experimental measurement [41]. The plasma length is defined as the distance from the beam focus to the maximum elongation of the plasma along the optical axis. The laser at wavelength 1064 nm of pulse width 30 ps is focused to a spot with diameter $2w_{0R} = 4.7$ μm inside the water with a focusing angle 22°. It is seen that the plasma length increases with the increasing pulse energy. In the inset of Fig. 3, the plasma length is also plotted as a function of $(\beta - 1)$ on a double-logarithmic scale. The moving breakdown model [13] predicts a square-root dependence of the plasma length versus the pulse energy as $z_{max} = z_R\sqrt{\beta - 1}$. Following this principle, the results in the log-scale should fit into a straight line with a slope 0.5. From the inset, it is observable that the present numerical results yield a straight line with a slope 0.517; while the experimental data in the inset can be least-square linearly fitted with a slope around 0.532 [41].

Figure 4 illuminates the dynamic process of plasma breakdown in distilled water induced by a 30 ps laser pulse with a focusing angle 22° at wavelength 1064 nm and with a super-threshold energy $\beta = 20$. The focal spot size is $2w_{0R} = 4.7$ μm. Figure 4(a) plots the free electrons gen-

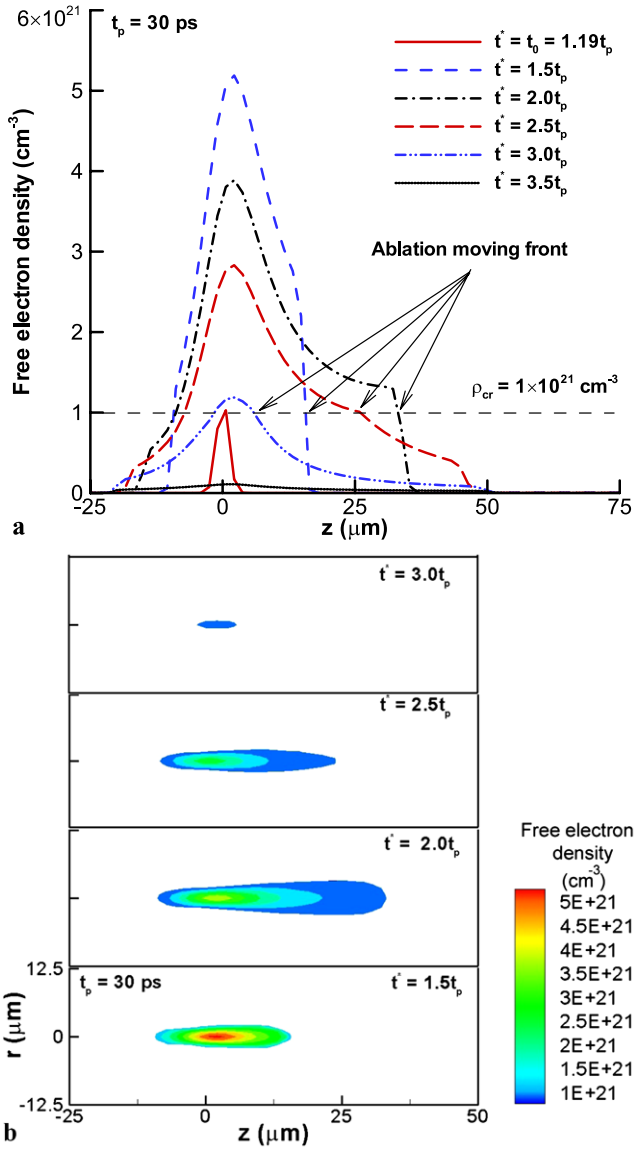

Fig. 4 Free-electron distributions at various time instants in water induced by a 30 ps pulse ($\lambda = 1064$ nm, $\theta_R = 22°$, $\beta = 20$, $\sigma_{ap} = 180\ \text{cm}^{-1}$ and the light is incident from right): (**a**) Along the optical axis ($r = 0$); and (**b**) contours of the free-electron distribution

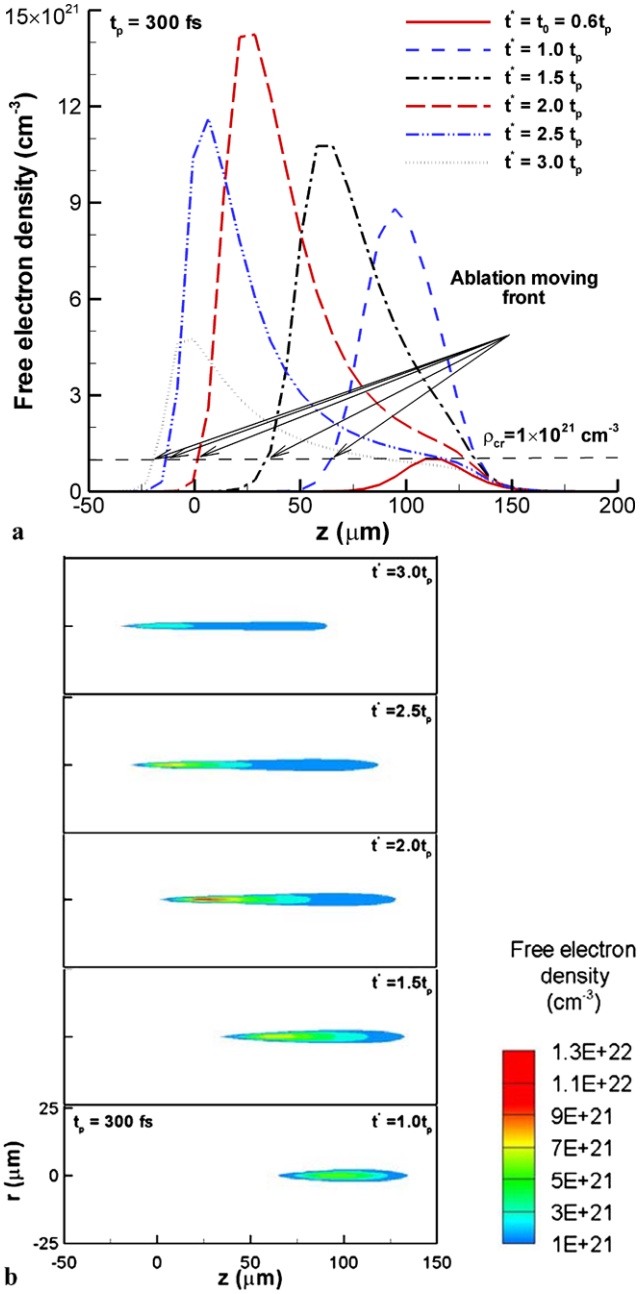

Fig. 5 Free-electron distributions at various time instants in water induced by a 300 fs pulse ($\lambda = 580$ nm, $\theta_R = 16°$, $\beta = 20$, $\sigma_{ap} = 360\ \text{cm}^{-1}$ and the light is incident from right): (**a**) Along the optical axis ($r = 0$); and (**b**) contours of the free-electron distribution

erated along the optical axis at six time instants, starting from the initial time (t_0) when optical breakdown occurs. Figure 4(b) shows the contours of the free-electron density at four specified ablation time instants. The time scale in Figs. 4 and 5 is defined as $t^* = t - z_0/c$, i.e., the time when the pulse front reaches the focus is $t^* = 0$, and when the pulse peak reaches the focus is $t^* = 2t_p$, respectively. From Fig. 4(a) it is seen that optical breakdown occurs at $t^* = 1.19t_p$, before the laser peak power reaches the focus. This is because the irradiation is super-threshold and the irradiation value can be over the threshold before peak. The breakdown originates from the focus because most of the laser energy is first accumulated there. Then the plasma formation is characterized by a rapid growth from the focus towards the incoming laser beam (see the curves and contours at $t^* = 1.5t_p$ and $t^* = 2.0t_p$), because the super-threshold laser irradiance at the locations in the upstream of the focus can be developed above the breakdown threshold for the picosecond Gaussian-profile pulse. Once the optical breakdown starts, the entire region is divided into two

sub-regions: non-breakdown region and breakdown region separated by a distinct ablation front (defined by the cut-off of the critical density). From Fig. 4(b) it is seen that the plasma cloud expands initially because of the occurrence of cascade ionization with more laser energy being input into the plasma cloud vicinity. With further lapse of time (after $t^* > 2.0t_p$), the ablation front retreats and the ablation plasma cloud shrinks (see the contours at $t^* = 2.5t_p$ and $t^* = 3.0t_p$), due to the decrease of laser irradiance and free-electron losses. Although the free electrons still keep propagating upstream as time advances, there is no optical breakdown ahead of the ablation front. It is also worth mentioning that little plasma develops one Rayleigh length ($z_R = 21.7$ μm) behind the laser focal center, as most of the laser light is already absorbed by the plasmas produced prior to and in the focal volume. This is the so-called plasma shielding property.

Next let us consider breakdown in distilled water with a 300 fs pulse at wavelength 580 nm. Figures 5(a) and (b) plot the free-electrons generated along the optical axis and the contours of plasma formation at various time instants, respectively. The laser has a super-threshold pulse energy $\beta = 10$ with a focusing angle 16°. The focal spot size is $2w_{0R} = 4.7$ μm. As shown in Fig. 5(a), optical breakdown begins at $t_0 = 0.6t_p$ in an upstream location, $z = 113$ μm. This location is behind the pulse peak location ($z = 1.4ct_p = 95$ μm) because of the delay existed between cascade ionization and multiphoton ionization. This time delay will be shown in Fig. 7 in detail later. From both Figs. 5(a) and (b), it is very clear that the ablation front moves towards the focus and finally exceeds the focus at time instants $t^* = 2.5t_p$ and $t^* = 3.0t_p$. This is in contrast with the behavior of the 30 ps laser ablation as shown in Fig. 4 where ablation front develops from the focus towards the incoming laser. At time instant $t^* = 2.0t_p$, the plasma length is extended to approximately 125 μm. We know that the laser pulse length is a product of the speed of light ($c = 0.226$ μm/fs in water) and the pulse duration. The 300 fs pulse yields a length value 68 μm. Hence, the plasma length observed in the breakdown region is longer than the laser pulse length at some time period. From Fig. 5(b) it is observed that the plasma cloud expands in the time period from $t^* = 0$ to $2.5t_p$, and then shrinks (comparing the case at $t^* = 3.0t_p$ with the case at $t^* = 2.5t_p$).

The difference of the plasma front moving directions induced by picosecond pulses and femtosecond pulses was discovered by Hammer et al. [43] as well. For 30 ps pulses, the pulse length 6.8 mm is much larger than the Rayleigh length ($z_R = 21.7$ μm), which means the spatial dependence of the irradiance dominates. The maximum irradiance is always at the beam focus. The irradiance at the beam focus will reach threshold essentially before any other point along the optical axis. Thus, at super-threshold laser irradiance, breakdown is predicted to begin at the beam focus and to move back towards the laser during the pulse, i.e., in the opposite direction of pulse propagation. For femtosecond pulses, however, the temporal dependence of the irradiance dominates. The irradiance may not be largest at the beam focus at a given time. The irradiance may exceed breakdown threshold prior to reaching the beam focus owing to the narrow temporal profile. For example, laser light travels 68 μm in 300 fs in water, a distance comparable with the Rayleigh length ($z_R = 44.0$ μm). Hence, for femtosecond pulses at super-threshold laser irradiance, breakdown is predicted to begin before the beam focus and to move forward to the focal plane during the pulse, i.e., in the direction of pulse propagation.

Now the study on plasma-mediated ablation is extended to the model skin tissue. A focused laser beam was incident on the surface of the epidermis or inside the skin tissue. A USP laser system at wavelength 1552 nm with pulse width 900 fs is considered. The critical free-electron density was estimated in the orders of 10^{18}–10^{20} cm^{-3} [1, 36]. The upper limit is given by the requirement that the plasma frequency $\omega_p = \sqrt{e^2\rho/m_e\varepsilon_0}$ must remain below the light frequency ω in order to effectively couple energy into the plasma. At electron densities greater than $\rho = \omega^2 m_e\varepsilon_0/e^2$, the plasma become highly reflective, and the incoming laser light leads to growth of the plasma volume rather than the free-electron number [9]. The upper limit of the free-electron density is approximately 4.7×10^{20} cm^{-3} at 1552 nm; and based on this limit value the breakdown threshold, $I_{th} = 5.1 \times 10^{11}$ W/cm^2, could be determined.

To study the ablation in a biological tissue, the attenuation of lights caused by the absorption and scattering effects needs to be accurately taken into account. Concerning with the strong 'directionality' coming from the focused beam propagation, the ray effects related to the angular discretization in the solution of the equation of radiative transfer should be examined. Figure 6 compares such an effect on the incident radiation profile in the focal plane at a time instant $t/t_p = 2$ for the various numerical schemes used. The dimensionless incident radiation is defined as $G^* = G/I_0(z = 0)$. The laser pulse is converged to the interface between the epidermis and dermis layers, which is about 0.5 mm deep. It is seen that the differences between the profiles of the incident radiation G^* predicted by the five schemes are very slight in the focal spot region and all these profiles gradually reach to the result predicted by the S_{16} scheme. However, differences are noticed in the wing area beyond 1.5 times of the beam radius. The radiation in this region mainly comes from the scattering effect and precise radiative transfer modeling is required. The number of the discrete ordinates associated with the S_N approximation is $n = N(N + 2)$. For example, the total number of the discrete ordinates is 80 for the S_8 scheme and 288 for the S_{16}

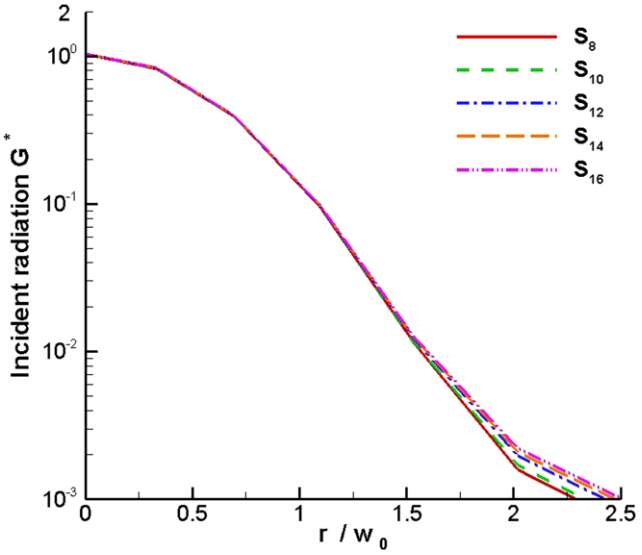

Fig. 6 Influences of the angular discrete order on the radial profile of the dimensionless incident radiation in the focal plane at the time instant $t = 2t_p$

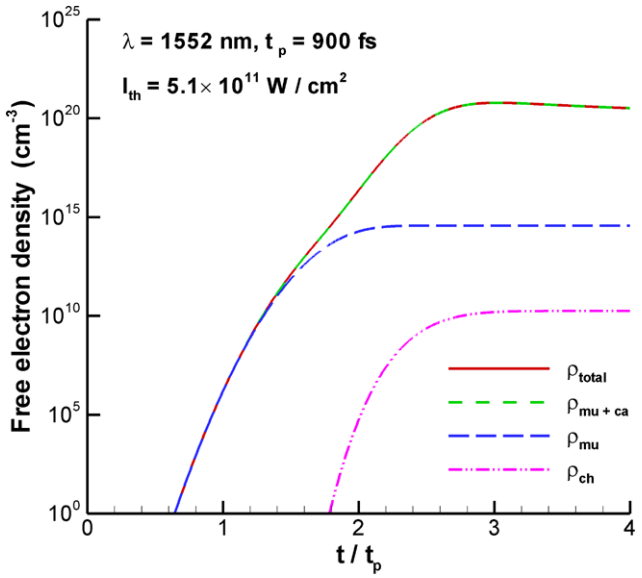

Fig. 7 Evolution of the free-electron density for different ionization mechanisms with breakdown threshold on the skin surface

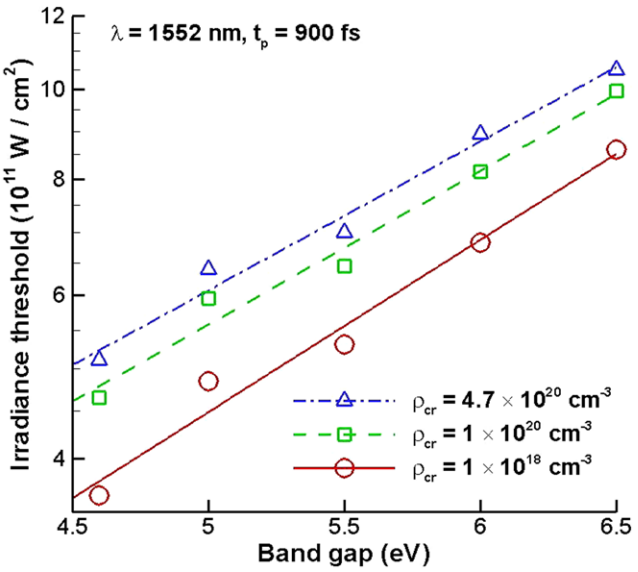

Fig. 8 Influences of the critical electron density and band gap on the ablation threshold

scheme, respectively. With the increase of the discrete order N, the ray effect lessens; but the required CPU time and memory increase nonlinearly. For instance, the calculation time is about 2 hours for the S_8 scheme; but it is extended to approximately 40 hours for the S_{16} scheme if the same grid size (200×100) is adopted for the two cases. In this study the S_{12} scheme is generally used as a compromise between the computation cost and the refinement of the discrete ordinates.

Figure 7 compares the effects of different pathways on ionization at the surface of the epidermis by the 900 fs pulse. The pink dash-double-dot curve stands for the effect by the chromophore ionization only. The blue long-dash curve represents the multiphoton ionization only. The green short-dash curve is for the combined multiphoton and cascade ionizations. The red solid curve accounts for all the ionization mechanisms. Multiphoton and chromophore ionization processes are two pathways to generate seed electrons. As expressed in (10)–(12), the multiphoton ionization rate is proportional to G^k and the chromophore ionization rate depends on the absorption of laser pulse energy $\sigma_a F(t)$. Once the first free electron appears in the calculation control volume the cascade ionization is assumed to take place, which leads to multiplication of free electrons by several orders of magnitude in a short time as shown in the green short-dash curve in Fig. 7. After that, the cascade ionization dominates the ionization process until the exponential growth of the free-electron density is slowed down by the electron-ion recombination. From Fig. 7 it is seen that the multiphoton ionization occurred at the peak irradiation ($t = 2t_p$), but the peak of the cascade ionization delayed about $0.8t_p$. The free-electron density increased by several orders after the occurrence of the cascade ionization, leading to plasma-mediated ablation. The chromophore ionization does not contribute too much to the generation of the seed electrons because of the relatively weak absorption of the chromophores ($\sigma_a = 1.85$ mm^{-1}) at wavelength 1552 nm. Thus, the multiphoton and cascade ionizations are the primary mechanisms for the USP laser ablation on the model skin tissue. It should be pointed out that in the present calculation, the properties of the chromophores are assumed to be the same as the melanosome [19].

The influences of the critical free-electron density and the ionization energy band gap on the threshold for the abla-

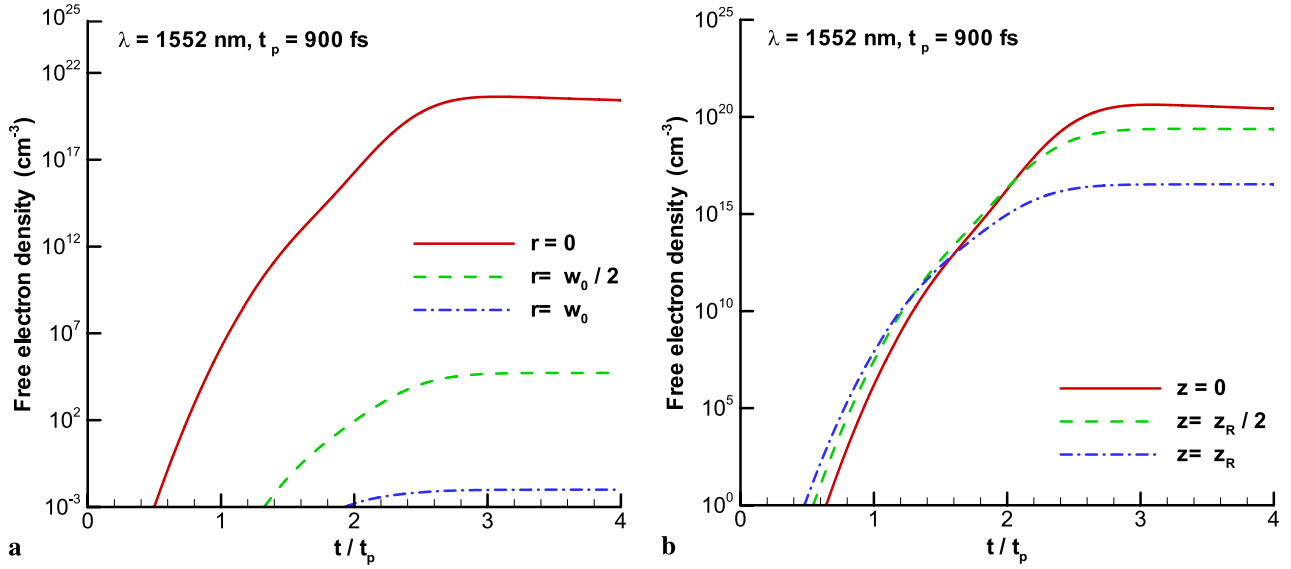

Fig. 9 Evolution of the free-electron density with breakdown threshold at the interface between the epidermis and dermis layers: (**a**) At the focal plane ($z = 0$); and (**b**) along the optical axis ($r = 0$)

tion on the epidermis tissue are investigated and plotted in Fig. 8. The discrete symbols in the figure represent the irradiance thresholds calculated by the present model while the continuous lines are obtained by least-square linear fitting of the calculated data. Different ionization energies, ranging from 4.6 to 6.5 eV, are selected to predict the irradiance threshold. It is observed that the laser irradiance threshold increases with increasing band gap and/or increasing critical free-electron density. The energy band gap plays a profound role in the determination of the threshold for optical breakdown.

To effectively remove the cancerous cells existing in the basal layer, a laser beam can be focused inside the skin to the dermis surface, which is about 0.5 mm deep. Here we consider plasma breakdown produced by a 900 fs pulse at wavelength 1552 nm with a focal spot size $2w_0 = 8.0$ μm. The threshold laser energy required for inducing optical breakdown at 0.5 mm beneath the skin surface is 370.58 nJ, much greater than that for generating ablation on the epidermis surface which is $E_{\text{th}} = 47.97$ nJ (corresponding to $I_{\text{th}} = 5.1 \times 10^{11}$ W/cm^2). This is because it is necessary to consider the attenuation of light intensity due to the absorption and scattering effects of the tissue.

Figure 9(a) shows the evolution of the free-electron density at three different radial locations along the focal plane at the dermis surface with the threshold laser irradiation. It is observable that less free electrons are generated with increasing radial location. For example, the maximum free-electron density generated at the center of the laser focus ($r = 0$) is the threshold value at 4.7×10^{20} cm^{-3}; while the maximum density at the position $r = w_0/2$ is reduced to the order of $\rho \sim 10^5$ cm^{-3}. At the edge of the beam waist ($r = w_0$), the free-electron density is very small and actually there exists no free electron.

Figure 9(b) shows the evolution of the free-electron density at three different optical axial locations (with $r = 0$), at the focus ($z = 0$) and in front of the focus ($z = z_{\text{R}}/2$ and $z = z_{\text{R}}$, respectively). The Rayleigh length z_{R} is calculated to be 45.34 μm. Since a human skin is very turbid against optical wavelength, the laser energy is quickly attenuated in the propagation direction. This could be a big shortcoming for using collimated laser beams. When the focused laser beam technology is adopted, however, the radiation intensity in the focus could be the maximum as demonstrated in a recent publication of the present authors [33]. From Fig. 9(b), it is seen that the free-electron density still reaches to the maximum value at the focal spot. The free-electron density at the two locations before the focus cannot reach to the maximum value, which is the threshold for optical breakdown; and thus, it ensures that ablation occurs only at the focus.

4 Conclusions

In this work, a 2-D axisymmetric numerical model is established combining the ultrafast radiative transfer and the rate equation to investigate the transient process of plasma formation and optical breakdown in biological tissues. Tissue ablations are considered for using the USP lasers of pulse width in the range of picoseconds and femtoseconds. The focused laser beam technology is adopted and its propagation in the turbid medium is simulated via solving the transient equation of radiative transfer with the discrete ordinates method. The free-electron density is obtained via

solving the rate equation with the fourth-order Runge–Kutta method.

The plasma formation with super-threshold pulse energy in the ablation of water was studied. It is demonstrated that for optical breakdown generated by the picosecond pulses, the plasma grows from the laser beam focus towards the incoming beam; while for the femtosecond pulses, the plasma formation begins before the laser focus and the front moves with the laser pulse towards the focus. No plasma formation was found one Rayleigh length behind the laser focus due to plasma shielding effect. The ablation plasma cloud expands from the beginning of ablation occurrence until the time when the cascade ionization arrives maximum and then shrinks to termination when the irradiation pulse complete passes through the focus. The multiphoton ionization peaks at the peak irradiance; but the peak of cascade ionization lags behind the peak of multiphoton ionization.

The present model is validated via extensive comparisons with the experimental measurement and other numerical models available in the literature for ablation in water. Good agreements between the current simulation and the existing results were found. An obvious advantage of the current multi-dimensional model over the existing 1-D models is that it is able to provide the dynamic shape for the plasma formation, which can then be employed for comparison with the plasma photos taken in experiments. Another advantage is that the present model can accurately account for the absorption and scattering effects; and thus, can be used for ablation modeling in general media including highly scattering biological tissues.

The ablation threshold for the model skin tissue is defined when a critical free-electron density is realized. At 1552 nm, the critical density is 4.7×10^{20} cm^{-3}. The ablation threshold is then determined to be 5.1×10^{11} W/cm^2 for the 900 fs laser for the present model tissue. The ablation threshold increases with increasing ionization band gap. The influences of various ionization mechanisms including the multiphoton, chromophore and cascade ionization pathways on the process of plasma generation for the model skin tissue are investigated. It is concluded that the multiphoton and cascade ionizations are the primary mechanism for inducing the USP laser plasma ablation in the tissue. The ray effect due to the limited angular discretization in simulation is found to be small in the focal region for the considered numerical schemes. When the focused beam is utilized, ablation can be well controlled to occur just in the focal spot. Thus, the possible ray effect in radiation modeling should not be a concern for ablation simulation.

Acknowledgements This material is based upon work supported by the National Science Foundation under Grant No. CBET-0827473. The authors appreciate Professor Alfred Vogel for valuable discussion with respect to his published numerical and experimental data on the laser induced breakdown in water.

References

1. Y.R. Shen, *The Principles of Nonlinear Optics* (Wiley, New York, 1984)
2. J. Kasparian, J. Solle, M. Richard, J.-P. Wolf, Appl. Phys. B **79**, 947 (2004)
3. K. König, I. Riemann, P. Fischer, K. Halbhuber, Cell. Mol. Biol. **45**, 195 (1999)
4. K. Schutze, G. Lahr, Nat. Biotechnol. **16**, 737 (1998)
5. W. Tao, J. Wilkinson, E.J. Stanbridge, M.W. Berns, Proc. Natl. Acad. Sci. USA **84**, 4180 (1987)
6. R.R. Anderson, J.A. Parrish, Science **220**, 524 (1983)
7. M. Beatrice, T. Alora, R.R. Anderson, Lasers Surg. Med. **26**, 108 (2000)
8. I. Itzkan, D. Albagi, M.L. Dark, L.T. Perelman, C. von Rosenberg, M.S. Feld, Proc. Natl. Acad. Sci. USA **92**, 960 (1995)
9. J. Noack, A. Vogel, IEEE J. Quantum Electron. **35**, 1156 (1999)
10. A. Vogel, V. Venugopalan, Chem. Rev. **103**, 577 (2003)
11. A. Vogel, J. Noack, G. Hüttmann, G. Paltauf, Appl. Phys. B **81**, 1015 (2005)
12. M.H. Niemz, E.G. Klancnik, J.F. Bille, Lasers Surg. Med. **11**, 426 (1991)
13. F. Docchio, P. Regondi, M.R.C. Capon, J. Mellerio, Appl. Opt. **27**, 3661 (1988)
14. F. Docchio, P. Regondi, M.R.C. Capon, J. Mellerio, Appl. Opt. **27**, 3669 (1988)
15. C.H. Fan, J. Sun, J.P. Longtin, J. Heat Transf. **124**, 275 (2002)
16. J. Zhou, J.H. Chen, Y. Zhang, Appl. Phys. B **90**, 141 (2008)
17. F. Williams, S.P. Varma, S. Hillenius, J. Chem. Phys. **64**, 1549 (1976)
18. M.S. Hutson, X.Y. Ma, Phys. Rev. Lett. **99**, 158104 (2007)
19. Q.Y. Fang, X.H. Hu, IEEE J. Quantum Electron. **40**, 69 (2004)
20. F.H. Loesel, J.P. Fischer, M.H. Götz, C. Horvath, T. Juhasz, F. Noack, N. Suhm, J.F. Bille, Appl. Phys. B **66**, 121 (1998)
21. H. Huang, Z. Guo, J. Micromech. Microeng. **19**, 055007 (2009)
22. H. Huang, Z. Guo, J. Phys. D, Appl. Phys. **42**, 165204 (2009)
23. H. Huang, Z. Guo, Lasers Med. Sci. **25**, 517 (2010)
24. Y. Yamada, Annu. Rev. Heat Transf. **6**, 1 (1995)
25. Y. Yamada, Opt. Rev. **7**, 366 (2000)
26. K. Mitra, S. Kumar, Appl. Opt. **38**, 188 (1999)
27. K.H. Kim, Z. Guo, Numer. Heat Transf. A **46**, 23 (2004)
28. Z. Guo, S. Kumar, Appl. Opt. **40**, 3156 (2001)
29. Z. Guo, S. Kumar, J. Thermophys. Heat Transf. **16**, 289 (2002)
30. Z. Guo, S. Kumar, K.-C. San, J. Thermophys. Heat Transf. **14**, 504 (2000)
31. Z. Guo, S. Kumar, Numer. Heat Transf. B **39**, 371 (2001)
32. Z. Guo, J. Aber, B. Garetz, S. Kumar, J. Quant. Spectrosc. Radiat. Transf. **73**, 493 (2002)
33. J. Jiao, Z. Guo, Phys. Med. Biol. **54**, 4225 (2009)
34. Z. Guo, S. Maruyama, Int. Commun. Heat Mass Transf. **26**, 997 (1999)
35. Z. Guo, S. Kumar, Appl. Opt. **39**, 4411 (2000)
36. P.K. Kennedy, IEEE J. Quantum Electron. **31**, 2241 (1995)
37. F. Docchio, Europhys. Lett. **6**, 407 (1988)
38. K. Nahen, A. Vogel, IEEE J. Sel. Top. Quantum Electron. **2**, 861 (1996)
39. E. Salomatina, B. Jiang, J. Novak, A.N. Yaroslavsky, J. Biomed. Opt. **11**, 261 (2006)
40. H. Ding, J.Q. Lu, W.A. Wooden, P.J. Kragel, X.H. Hu, Phys. Med. Biol. **51**, 1479 (2006)
41. A. Vogel, K. Nahen, D. Theisen, J. Noack, IEEE J. Sel. Top. Quantum Electron. **2**, 847 (1996)
42. A. Sollier, L. Berthe, R. Fabbro, Eur. Phys. J., Appl. Phys. **16**, 131 (2001)
43. D.X. Hammer, E.D. Jansen, M. Frenz, G.D. Noojin, R.J. Thomas, J. Noack, A. Vogel, B.A. Rockwell, A.J. Welch, Appl. Opt. **36**, 5630 (1997)